Constraining Time Variations in Enceladus's Water-vapor Plume with Near-infrared Spectra from Cassini's Visual and Infrared Mapping Spectrometer

K. E. Denny[1], M. M. Hedman[1] , D. Bockelée-Morvan[2], G. Filacchione[3] , and F. Capaccioni[3]

[1] Department of Physics, University of Idaho, Moscow, ID 83844, USA
[2] Observatoire de Paris, Université Paris-Diderot, Paris, 75010, France
[3] Istituto di Astrofisica e Planetologia Spaziali, Rome, 00133, Italy

Abstract

Water vapor produces a series of diagnostic emission lines in the near-infrared between 2.60 and 2.75 μm. The Visual and Infrared Mapping Spectrometer (VIMS) on board the Cassini spacecraft detected this emission signal from Enceladus's plume, and so VIMS observations provide information about the variability of the plume's water-vapor content. Using a data set of 249 spectral cubes with relatively high signal-to-noise ratios, we confirmed the strength of this water-vapor emission feature corresponds to a line-of-sight column density of order 10^{20} molecules m^{-2}, which is consistent with previous measurements from Cassini's Ultraviolet Imaging Spectrograph. Comparing observations made at different times indicates that the water-vapor flux is unlikely to vary systematically with Enceladus's orbital phase, unlike the particle flux, which does vary with orbital phase. However, variations in the column density on longer and shorter timescales cannot be ruled out and merit further investigation.

Unified Astronomy Thesaurus concepts: Enceladus (2280); Infrared spectroscopy (2285); Volcanism (2174); Water vapor (1791); Saturnian satellites (1427)

Supporting material: data behind figure

1. Introduction

Saturn's moon Enceladus is an exceptionally interesting object because it is geologically active, producing a plume of predominantly water-ice grains. Multiple instruments on board Cassini observed both the particulate and vapor components of the plume material emerging from four fissures (tiger stripes) located near the south pole of the moon (see Schenk et al. 2018 for recent reviews). Observations of this material have aided in the understanding of the geological processes occurring on Enceladus; however, there are still many questions about how the plume's activity varies over time.

Variations in Enceladus's activity on various timescales can provide insights into what is happening beneath the moon's surface. Fluctuations in the plume particle flux have been extensively studied using Cassini's Visual and Infrared Mapping Spectrometer (VIMS; Hedman et al. 2013; Sharma 2023) and Imaging Science Subsystem data (Nimmo et al. 2014; Ingersoll et al. 2020). These studies show that the overall brightness and particle output of the plume are correlated with Enceladus's position along its eccentric orbit. Specifically, the plume's brightness peaks when Enceladus is farthest from Saturn in its orbit (Hedman et al. 2013; Ingersoll et al. 2020). These trends indicate that the particle flux is correlated with the tidal stresses experienced by Enceladus's south polar terrain (Hurford et al. 2009; Nimmo et al. 2014).

The plume's water-vapor variations have been significantly more difficult to document because the water vapor is most clearly observed in relatively short and infrequent observations like occultations and close flybys. This has led to a debate about whether the vapor plume varies on orbital timescales correlated with the particulate component or if it is relatively constant. Occultation data obtained by Cassini's Ultraviolet Imaging Spectrograph (UVIS) indicate that there is a constant vapor flux throughout Enceladus's orbit (Hansen et al. 2020). However, data collected by Cassini's Ion and Neutral Mass Spectrometer during close flybys provide evidence of variations in the plume's gas jets (Saur et al. 2008; Smith et al. 2010; Teolis et al. 2017).

Enceladus's water-vapor flux can potentially be monitored over a broader range of conditions using near-infrared emission lines. Such lines were recently observed by the James Webb Space Telescope (JWST; Villanueva et al. 2023), but there is evidence that VIMS can see them as well (Dhingra et al. 2017). This paper will use the VIMS observations to constrain the water-vapor content of the plume over the course of the Cassini mission. Section 2 will discuss the format of the VIMS plume data and the methods we used to isolate the water-vapor signal. Section 3 will demonstrate that the signal in the VIMS data is consistent with a real water-vapor feature using model-based predictions. Finally, we use this feature to calculate line-of-sight column density measurements over the course of the Cassini mission in Section 4.

2. Cassini-VIMS Plume Data

VIMS obtained observations of Enceladus and its plume at 352 wavelengths between 0.35 and 5.2 μm that are packaged as spectral cubes containing two spatial dimensions and one spectral dimension (Brown et al. 2004). We used calibration file RC19 and standard routines to convert the raw signal levels to a standard measure of reflectance called I/F. We computed geometrical parameters like Enceladus's orbital phase (i.e., mean anomaly) based on the time stamp for each observation. It is worth noting that a spectral shift of ~10.4 nm or 0.71
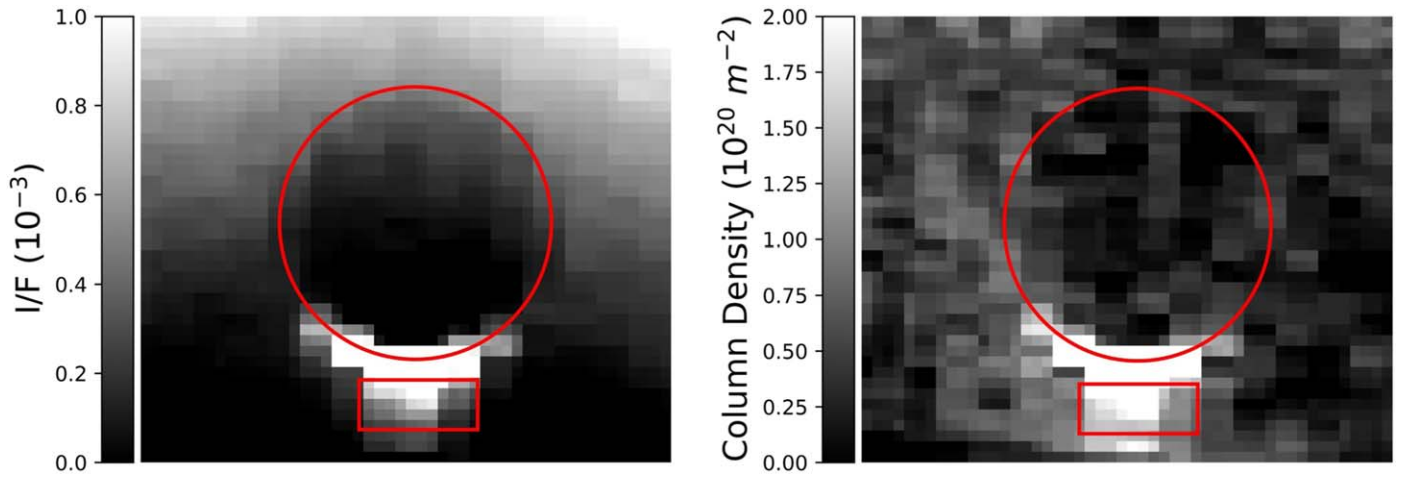
Figure 1. Left: map of the plume's brightness at 2.70 μm derived from an average of five VIMS cubes (V1511798376, V1511800181, V1511800741, V1511801493, and V1511802247). Note that this brightness is mostly due to reflected sunlight from Enceladus's lit limb and the plume particles. The image is reprojected on a grid with 19 km pixel^{-1} and oriented so that the plume points downward. Right: map of the water-vapor column density derived from the same averaged image. Column densities were calculated using the average residual values and Equation (1). Note that regions of high column density are visible outside the region where the plume particles are bright, which provides evidence that this signal traces a different plume component. The red circles outline Enceladus, and the red rectangles show the pixels used for the spectral analysis (see Section 2).

channels occurs over the course of the 13 yr Cassini mission (Clark et al. 2018). This spectral shift is almost negligible for this study because the low signal-to-noise ratio (S/N) and limited spectral resolution of VIMS cubes means that the narrow emission lines are not clearly resolved.

In order to facilitate comparisons among the various plume observations, the data from the infrared channel for each of these cubes were reprojected onto a uniform coordinate system aligned with Enceladus's spin axis and centered on the moon itself (Hedman et al. 2013). An example of the data found in these cubes is shown in Figure 1. The left panel shows a map of the plume's brightness in the 2.60–2.75 μm wavelength band, which encompasses the ν_1 and ν_3 vibrational bands of H_2O (Bockelée-Morvan et al. 2015). This map is based on an average of five reprojected VIMS cubes, and the bright particle plume is visible extending below Enceladus's south pole. Note that these particular cubes were originally obtained in a mode where each pixel was 0.25×0.5 mrad (Hedman et al. 2009), so these pixels appear elongated in the horizontal direction after being reprojected.

While there are a few situations where the water-vapor signal is strong enough to be spatially mapped (Figure 1, Right panel; see Section 3.3 for more details), for most of the VIMS observations, we can only achieve sufficient S/N to quantify the water-vapor content of the plume by averaging all the data with the region containing the plume. To ensure consistency, we define the plume area as a region containing 55 pixels in the reprojected cubes covering altitudes $\sim$30 to $\sim$130 km below Enceladus's south pole and within $\sim$120 km of the moon's spin axis (see red rectangles in Figure 1). These ranges were selected to avoid contamination from Enceladus's lit limb while still capturing altitudes where the water-vapor signal is expected to be strongest. In particular, the UVIS occultation data indicates that water-vapor column density is strongest at altitudes below 100 km (Hansen et al. 2020). To remove instrumental backgrounds, we subtract the mean signal in a 9 pixel region centered at $\sim$330 km from Enceladus's spin axis and $\sim$20 km

below the south pole. To filter outliers in each cube's average plume spectra, we also calculated standard deviations within each spectral channel and discarded reflectance I/F values more than 2σ away from the median when computing these averages. Finally, we exclude all data in spectral channel 2.564 μm because it consistently contains outliers throughout the data set even though this channel is not defined as a hot pixel in the VIMS documentation (Clark et al. 2018).

To ensure consistency among our estimates of the plume signal, we only considered cubes that fully covered the selected region and were obtained at distances within 300,000 km of Enceladus. There were 249 cubes spanning a range of orbital phases and observation times meeting these criteria, which are listed as groups in Table 1 and analyzed individually in Section 4.

3. Evidence of a Water-vapor Emission Feature

The water-vapor signal in the VIMS data is relatively subtle because the instrument's limited spectral sampling ($\approx$16.6 nm band^{-1}) does not allow individual lines to be clearly resolved. Instead, the spectral radiance appears as a slightly elevated brightness between 2.60 and 2.75 μm that is superimposed on top of a background spectral slope due to reflected sunlight from the particles in the plume and E ring (Dhingra et al. 2017). We first noticed this slightly elevated brightness in these data in residuals from a Mie model fit to the spectra described in Appendix A. We therefore developed techniques to isolate the potential water-vapor signal from each cube that are described in Section 3.1 below. In addition, we verified that the relevant spectral feature could indeed be due to water-vapor emission by both comparing the average signal to predictions from the Planetary Spectrum Generator (PSG; see Section 3.2) and checking that the band area of this feature is consistent with the expected average column density of water vapor in the plume (see Section 3.3).

3.1. Isolating the Water-vapor Signal from the VIMS Plume Spectra

For this analysis, we will focus on the plume signals in the 2.484–2.850 μm wavelength range. These spectra include both the water-vapor signal between 2.60 and 2.75 μm and background trends due to the plume and E-ring particles. These background trends can conveniently be approximated by a low-order polynomial, so we can isolate the water-vapor signal by first defining three wavelength bands: 2.484–2.598 μm, 2.615–2.733 μm, and 2.748–2.850 μm. The middle band contains the eight wavelength channels where we would expect to find the water-vapor emission signal. In order to isolate this signal, we fit quadratic polynomials to the data in both surrounding bands (2.484–2.598 μm and 2.748–2.850 μm). These polynomial models are then subtracted from the spectra to produce residuals showing the intensity of water-vapor emission in the middle band for each cube. (We also performed cubic fits but found that these did not improve the results significantly.).

Figure 2 (top panel) shows the nonweighted average spectra of the plume as derived from the entire 249 cube data set (Table 1) and the resulting residual I/F brightness (middle panel). Note that a straight average was taken because potential variations in the strength of the water-vapor feature (see Section 4) are not properly accounted for using weights based on the error bars of individual spectral cubes. The error bars for this spectrum are therefore based on the root-mean-square residuals about the quadratic trend. The top panel of Figure 2 shows a strong slope that is well fit by a quadratic model and can be attributed to the water-ice absorption band in the reflected sunlight from the particles in the plume (Hedman et al. 2009; Dhingra et al. 2017). On top of this trend, a potential water-vapor signal is visible as a slight peak present around 2.60–2.75 μm. The middle panel shows the residual reflectance I/F after subtracting the quadratic fit from the spectra, which isolates the potential water-vapor emission feature.

3.2. Comparing the Observed Signal with Predictions from the PSG

In order to determine if the residual signal shown in Figure 2 is compatible with water-vapor emission, we compared our observed spectra with predictions from the PSG.[4] This tool can model spectral features based on various properties related to the celestial body, detector, composition, etc. (Villanueva et al. 2018). For this particular study, we assume the Enceladus plume acts similarly to an expanding coma from a comet and consists of only water molecules since estimates of the water-vapor abundance are within the 96%–99% range (Postberg et al. 2018). We use a water-vapor column density of 3.63×10^{19} m^{-2}, which is consistent with calculations provided in Section 3.3. To estimate the temperature of the water vapor, we assume a rapid cooling-off process occurs after the particles leave the tiger stripes where the interior temperature is estimated to be 197 ± 20 K (Goguen et al. 2013). Therefore, we use a temperature of 70 K for the models because this is the equilibrium temperature of ice at Saturn's distance from the Sun and it is consistent with the coldest temperatures seen on Enceladus's surface (Spencer et al. 2018). A full list of PSG input parameters can be found in Table 2 in Appendix B. The lower panel in Figure 2 shows PSG models from 2005, 2010, and 2015 compared to the average spectrum residual from all 249 spectral cubes (converted to units of radiance). The PSG model has been applied three times to take into account the reduction of solar flux due to the increase of the heliocentric distance from 9.1 to 10 au between 2005 and 2015. The spectral shift between the three PSG models shown in the plot corresponds to the wavelength shift in VIMS observations over the Cassini mission (Clark et al. 2018). A more detailed plot of this spectral channel shift can be found in Figure 6 in Appendix B. Comparing the average residual signal to the three PSG models shows that the shape and intensity of the detected signal are consistent with the predicted signal from water-vapor emission lines. This supports the hypothesis that this feature is a real signal from water vapor in the plume.

3.3. Comparing Water-vapor Column Densities with Other Measurements

Another way to validate the water-vapor signal is to estimate the column density of H$_2$O molecules along the line of sight using the following equation (Bockelée-Morvan et al. 2015):

$$\langle N \rangle = \frac{4\pi I_b}{h \nu g_f} \tag{1}$$

where I_b is the integrated band intensity [Wm^{-2} sr^{-1}] measured over the 2.615–2.733 μm wavelength range, h is Planck's constant, ν is the central frequency of the band, and g_f is the so-called g-factor or the band emission rate. For this particular band we used the g-factor from Bockelée-Morvan et al. (2015), which gives $g_f = 3.682 \times 10^{-4}$ s^{-1} at 1 au. To correct for distance, we divided this g-factor by r^2, where r is the range between Enceladus and the Sun at the time of each observation in astronomical units. To convert our residual values to band area, we used the calibration equations from Clark et al. (2018) and solar flux values from the National Renewable Energy Laboratory,[5] which are within 6.5% of Thekaekara's solar spectrum (Thekaekara 1973) used in the VIMS calibration pipeline. Solar flux values were corrected for the Sun's range during each observation.

The errors in the column density measurements are calculated using the standard deviation of residual spectral values in the surrounding wavelength bands (2.484–2.598 μm and 2.748–2.850 μm) and dividing by the square root of the number of spectral channels in the middle band. This should provide a relatively conservative estimate of the uncertainty in the column density that is robust against uncertainties in the models for the background and the signal.

The right panel of Figure 1 shows the computed column density for the spectral image produced by averaging five data cubes (V1511800181–V1511803001). This map shows that the water-vapor signal is more broadly distributed than the particle-plume signal, being visible farther below Enceladus and being noticeably wider than the particle-plume signal visible in the left panel of the same figure. This distinct spatial distribution provides further evidence that this is a real water-vapor signal.

---

[4] https://psg.gsfc.nasa.gov

[5] https://www.nrel.gov/grid/solar-resource/spectra-astm-e490.html

Table 1
Average Water-vapor Column Density for Each Observation Group

File Range	Date	Cubes n[a]	Exposure Time[b] (s)	Observation Duration[c] (hr)	α (°)	Range (km)	Orbital Phase[d] (°)	$\langle N \rangle$[e] (10^{19} m^{-2})	χ^2_{red}
V1511794087–V1511810387	2005-11-27	14	7.9	4.6	161.2	141372.6	102.5, 151.0	9.341.05	7.6
V1556120297	2007-04-24	1	0.4	0.1	155.4	184554.5	77.2	6.214.40	⋯
V1569822293–V1569824909	2007-09-30	8	5.1	0.8	156.1	185659.5	288.8, 296.4	6.771.19	4.4
V1635804522–V1635817738	2009-11-01	22	14.1	3.7	161.2	197151.8	153.0, 192.7	1.741.14	10.9
V1652826740–V1652830668	2010-05-17	12	7.7	1.1	156.6	264376.5	7.6, 19.6	5.120.97	4.8
V1660403219–V1660407931	2010-08-13	9	5.8	1.4	159.6	257005.5	336.5, 350.2	5.672.58	3.2
V1663878677–V1663881820	2010-09-22	12	7.7	0.9	162.3	249462.4	92.2, 101.7	−2.952.49	8.4
V1671552668–V1671567368	2010-12-20	12	7.4	4.4	157.6	133235.6	−1.7, 43.3	0.291.71	3.8
V1675101079–V1675111889	2011-01-30	41	26.2	3.1	152.6	215890	−27.3, 5.9	2.971.07	7.2
V1696147993–V1696155274	2011-10-01	24	15.4	2.1	150.2	187076.3	171.3, 193.4	4.400.75	9.3
V1697685856–V1697694716	2011-10-19	19	12.2	2.5	150.2	189015.8	162.4, 189.1	4.901.47	8.8
V1699226646–V1699231874	2011-11-05	15	9.6	1.5	149.3	190981.2	161.8, 177.5	6.291.32	5.1
V1711539317–V1711552021	2012-03-27	34	21.8	3.6	158.4	209498.1	115.2, 153.6	2.330.85	7.4
V1713081678–V1713090058	2012-04-14	21	13.4	2.4	158.2	208633.8	119.3, 144.6	3.141.38	7.7
V1823539171–V1823540036	2015-10-14	4	2.6	0.3	150.5	220495.3	54.2, 56.9	3.234.45	11.2
V1824760877	2015-10-28	1	0.6	0.1	141.8	210623.6	164.4	21.07.98	⋯

Notes.
[a] The number of spectral cubes in each observation group.
[b] The sum of the total exposure time per pixel for n cubes in the sequence.
[c] The duration window from the first observation to the last observation.
[d] The minimum and maximum orbital phases for each observation group.
[e] The weighted average group column density is $4.360.32 \times 10^{19}$ m^{-2}.

In addition, the average spectrum shown in the bottom panel of Figure 2 yields an estimated water-vapor column density of $3.63 \pm 0.40 \times 10^{19}$ m^{-2}, and for the individual observations, the observed signals require column densities of order 10^{20} molecules m^{-2} (see Section 4). These values are consistent with column density measurements made from occultation observations from Cassini's Ultraviolet Imaging Spectrograph, which gives values ranging from 9 to 15×10^{19} m^{-2} (Hansen et al. 2020). Villanueva et al. (2023) quote an average column density of $1.7 \pm 0.1 \times 10^{18}$ m^{-2} from recent JWST observations of Enceladus. The JWST column density is about an order of magnitude lower than ours because the comparatively low spatial resolution of JWST (each pixel being several hundred kilometers wide) means that it can only measure average column densities over broad regions of the plume. By contrast, our data come within a 100 km of the south polar terrain, where occultation measurements show the plume's column density is much larger (Hansen et al. 2020).[6]

4. Water-vapor Variations

Having established that VIMS was able to detect the water-vapor content of the plume, we can now use the VIMS observations to search for variations in Enceladus's water-vapor activity on a range of different timescales. Residual spectra similar to Figure 2 are computed on individual spectral cubes and used to estimate the number of H_2O molecules needed for each cube using the same procedures described in Section 3.3. As mentioned in Section 3.3, column density errors are calculated using the residuals from the quadratic fits to the background trend. We first use these estimates to

examine whether the water-vapor column densities vary systematically with orbital phase. Then we examine whether there could be variations in the column density on other timescales.

Figure 3 shows the column density measurements for all 249 spectral cubes in our filtered data set as a function of orbital phase, and the observations are color-coded by the years they were observed. Note that, while the data show substantial scatter, the column densities are on average positive, consistent with the detectable signal in the averaged data. However, there is no clear pattern in column density fluctuations with orbital phase.

The lower panel of Figure 3 shows the variations of the nonweighted average column density estimates of groups of spectral cubes obtained within similar observation times (see average spectral residuals in Appendix D), along with the estimated water-vapor column density measurements derived from UVIS occultation observations (Hansen et al. 2020; Table 1 provides the average column density values for each of these observation groups, along with other properties of the data subsets.) The UVIS and VIMS estimates are generally consistent with each other (although the UVIS numbers may be a bit higher on average than the VIMS numbers), and neither shows clear evidence for systematic variations with orbital phase. If the water-vapor flux varied with orbital phase like the particle flux, then the column density at orbital phases around 180° (where Enceladus is farthest from Saturn) would always be about 4 times larger than it is at other orbital phases (Nimmo et al. 2014; Ingersoll et al. 2020; Sharma 2023). We therefore agree with Hansen et al. (2020) that the water-vapor plume does not show the same systematic activity variations as the particle plume.

While Figure 3 indicates that there are no obvious trends with orbital phase, it is also important to look for evidence of longer-term variations among the different observations and

---

[6] Note that we do not provide estimates of outgassing rates of the plume material because these calculations require secure measurements of how the vapor plume's brightness varies with altitude, which is hard to extract from our data due to limited S/N.
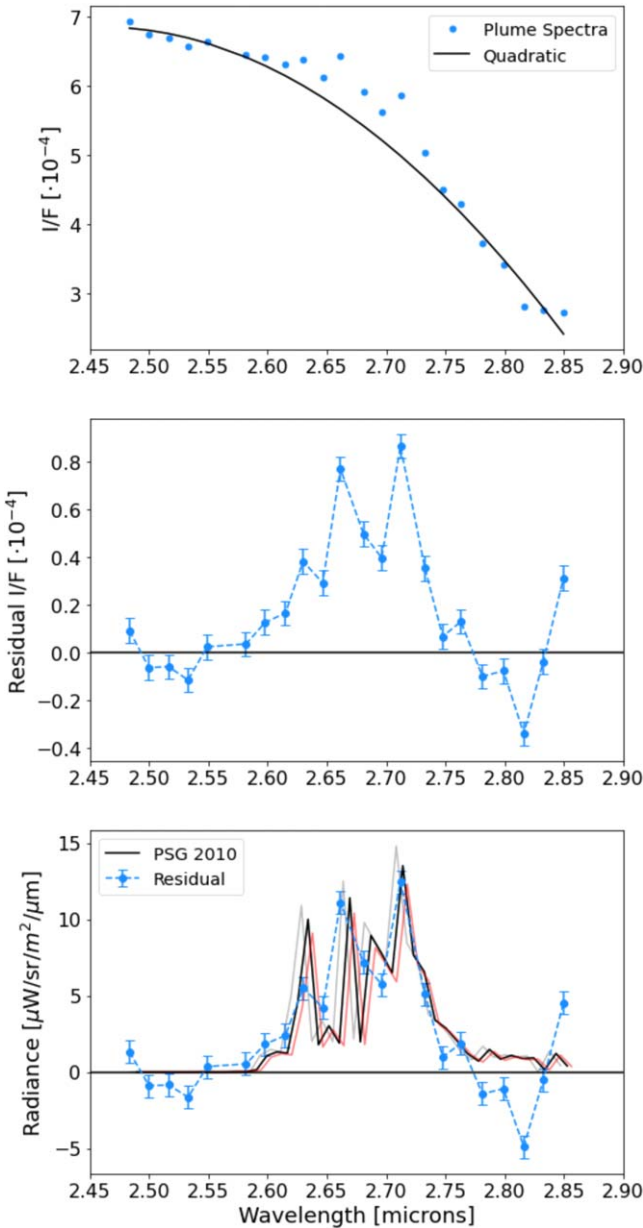
Figure 2. The average plume spectra and residual of 249 spectral cubes from Cassini-VIMS observed from 2005 to 2015. The top panel shows the background-subtracted average spectra along with a quadratic fit to the regions between 2.484–2.598 μm and 2.748–2.850 μm. The middle panel shows the residual brightness after subtracting the quadratic polynomial. The bottom panel shows the same plume residual compared to the PSG models for 2005 (gray), 2010 (black), and 2015 (red). The wavelength shift in the PSG models was applied using values from Clark et al. (2018). The models assume a column density of 3.63×10^{19} molecules m^{-2}, consistent with the best-fit column density based on the feature's band area (see Section 3.3).

short-term variations within each observation group. The column density estimates shown in Table 1 and the average residual signals for individual groups shown in Appendix D may reveal hints of yearly variations over the Cassini mission. The water-vapor flux seems to have been particularly high in the VIMS observations taken in 2005 and 2007. More explicitly, there are roughly eight groups that have 1σ error bars on the order of 1×10^{19} m^{-2} (see Table 1). Among these higher-quality observations, groups 2005 November 27 and 2007 September 30 have estimated column densities that are

$\sim 5\sigma$ above 0 and show signals around 2.7 μm that are consistent with those expected for the water-vapor flux feature (see Appendix D). By contrast, groups 2011 January 30, 2011 October 1, and 2012 March 27, despite also having error bars around 1×10^{19} m^{-2}, have lower column densities, with two of them being less than 3σ above 0. Assuming our error bars are accurate, this decline is marginally statistically significant because the average signal of the 2005 November 27 and 2007 September 30 observations is roughly $\sim 3\sigma$ above the average signal of the 2011 January 30, 2011 October 1, and 2012 March 27 observations. This implies that we have either underestimated our error bars by roughly a factor 2 or that the typical vapor flux may have been lower during the observations made in the latter part of the Cassini Mission.

In order to investigate shorter-term variations in the plume, we examined the column density estimates as a function of the orbital phase for each observation group. First, we calculated reduced χ^2 values for each observation group's estimated column density, which are provided in Table 1. Most of these reduced-χ^2 values greatly exceed 1, implying that the scatter among the observations within each group is roughly 2–3 times larger than expected, given the conservatively defined error bars. For all groups consisting of multiple spectral cubes, the probabilities to exceed associated with these reduced-χ^2 values are equal to or much less than 0.01%. It is therefore worth taking a closer look at these subsets of the data to see if there are any trends that could represent short-term variations. Figure 4 illustrates the water-vapor variations for four particularly interesting observation groups in our data set (the remaining observation group plots can be found in Appendix C).

First, the 2005 November 27 group plot shows observations that were previously studied in great detail in Hedman et al. (2009) due to their relatively high S/Ns (note that four out of the five observations between orbital phases of 120° and 130° show the water-vapor emission signal clearly in their individual spectra.). While the signal appears to be present in the majority of these cubes, the scatter among the observations is larger than their formal error bars, and the signal between 120° and 130° is on average higher than the observations between 100° and 110°.

The 2007 September 30 group shows evidence for a possible dip in the water-vapor flux between 294° and 296°, which spans a time of approximately 10 minutes. This feature appears unlikely to just be a statistical artifact because it is coherent and localized in time. Hence, unless this is due to some unidentified systematic artifact in the data, then it represents a very rapid fluctuation in the plume's water-vapor flux.

The 2011 October 1 group shows a possible increase in the vapor-plume activity between 185° and 195° in a duration of 30 minutes. If this increase is real, the rise in water-vapor flux after Enceladus passes apocenter is interesting because the particle flux would be decreasing in this orbital phase range (Ingersoll et al. 2020; Sharma 2023).

The 2012 March 27 group maps an interesting result that occurs between orbital phases 135° and 143°. The water-vapor output tends to bifurcate in this region between relatively large column density measurements and negative ones. Analysis of the individual spectra of the observations in this orbital phase range shows no clear cause for this odd pattern. While the S/Ns in this observation group are fairly low, some spectra exhibit clear emission peaks, while others do not.
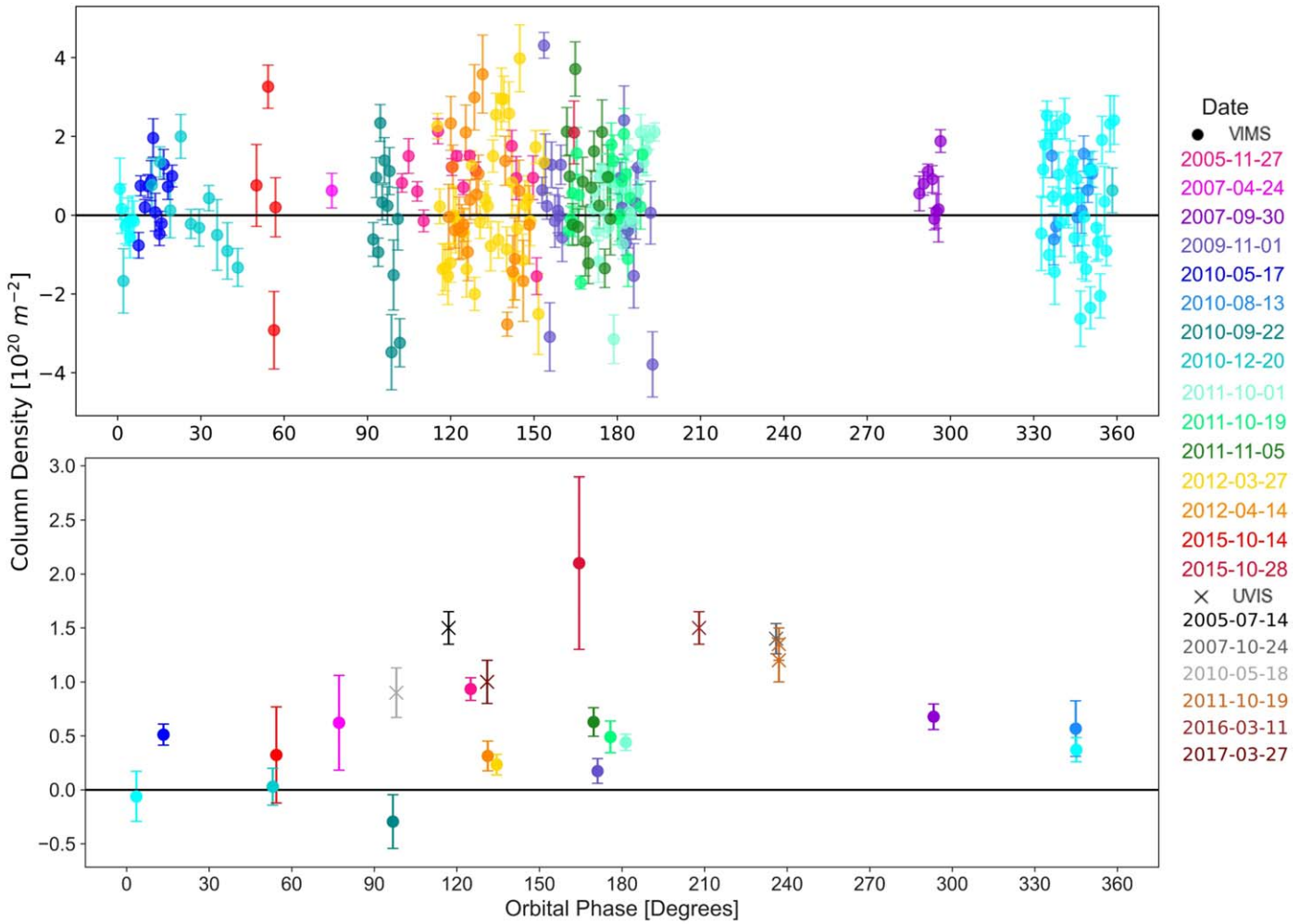
Figure 3. Changes in water-vapor column density as a function of Enceladus's orbital phase. The top panel shows the column density measurements for 249 spectral cubes with different colors representing the days in which the observations were taken. The bottom panel shows nonweighted average column density estimates for each observation group. Column density measurements of Enceladus's plume occultations observed by UVIS obtained from Hansen et al. (2020) are also shown. There is no evidence for a clear pattern of water-vapor column density variations over Enceladus's orbit. Note that although a small fraction of column densities in the top panel are negative, this is likely due to random noise because the signal-to-noise for individual measurements are relatively low. The fact that none of the averaged points in the lower panel are significantly negative is consistent with this idea. A full table of the estimated column densities and the observation properties of the individual cubes in the top panel is hosted by this figure and is available for download.

(The data used to create this figure are available.)

These data therefore provide some evidence that the plume's vapor activity can potentially vary on short timescales. Unfortunately, most of our groups do not have high enough S/Ns to adequately map such small-scale variations (see Figure 4, 2012 March 27), and even the variations shown in Figure 4 look to be somewhat stochastic. However, given we used relatively conservative error bars, our analysis suggests that $\leqslant 1$ hr variations in water-vapor column density cannot be excluded and merit further investigation, especially if additional observations from JWST become available.

Finally, we can note that the total data set of column densities shows an excess variance similar to or smaller than the variance of the individual groups (the overall reduced χ^2 for the entire data set being around 4). This result implies that while there are significant variations among the groups, these fluctuations are smaller than the variations within most of the observation groups, and so the variations among the groups could potentially be due to residual short-term variations.

5. Discussion

This analysis provides strong evidence that the 2.7 μm water-vapor emission feature is detectable in the Cassini-VIMS spectra of Enceladus's plume. These data are consistent with previous UVIS measurements of the plume's vapor column density and also confirm that the plume's vapor content does not vary dramatically with orbital phase. However, we also find hints that the plume's vapor content may vary on timescales as short as around an hour.

The results of this study confirm that there is a difference between the tidal variation of the plume's particle flux and the fluctuations in the plume's vapor content. This suggests that the variation in the water-vapor plume is complicated by other geological processes occurring within the fissures. Therefore, our detections of minimal variation over orbital phase and possible small-scale variations in observation groups could be consistent with individual plume jets turning on and off as suggested by Hansen et al. (2020) and studied by Portyankina et al. (2022). This
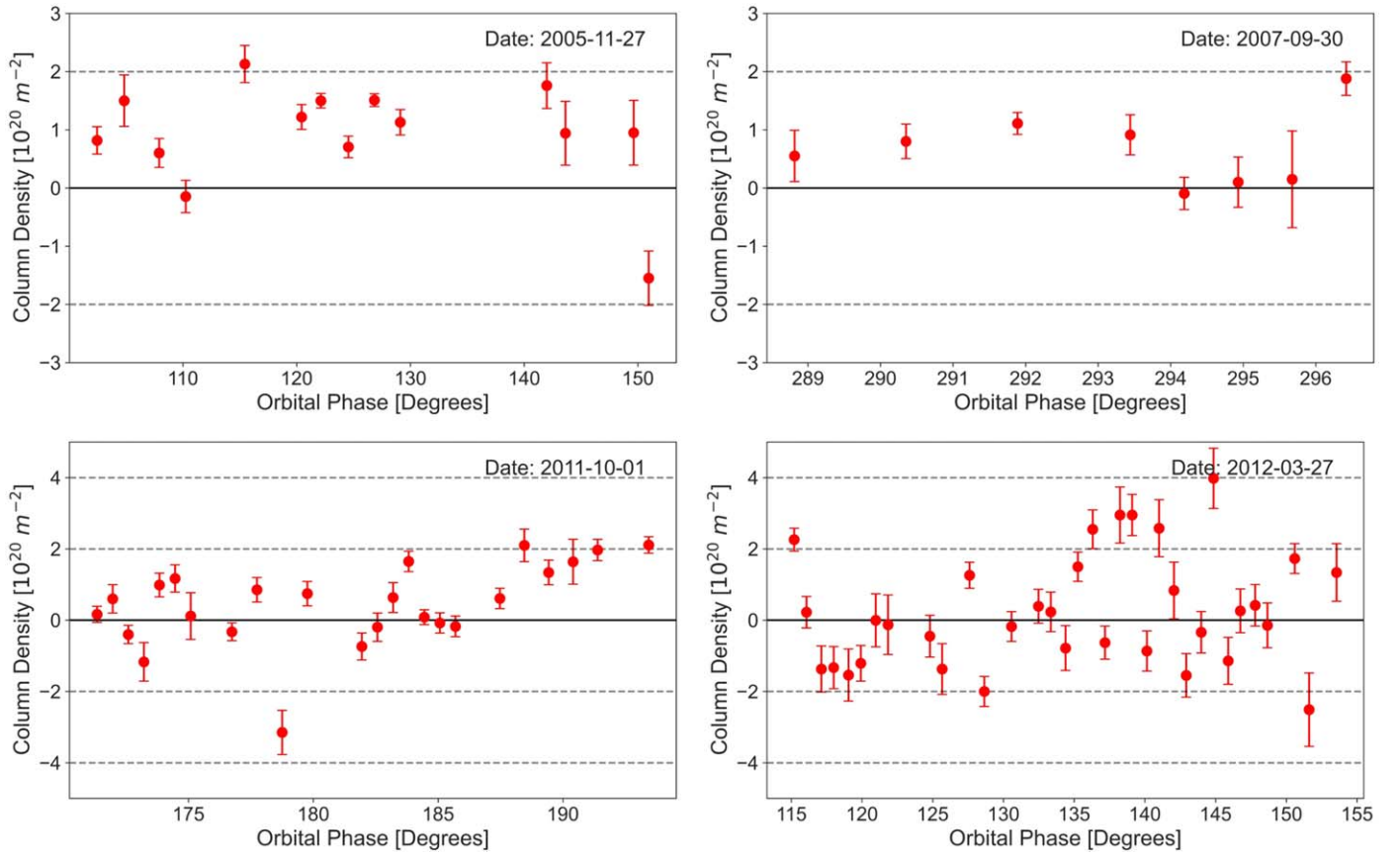
Figure 4. Column density variations plotted over the orbital phase in four different observation groups. 2005 November 27 Group: variations in the subset of observations analyzed in Hedman et al. (2009). With good signal-to-noise ratios, this group consistently shows the water-vapor signal in the middle five observations. 2007 September 30 and 2011 October 1 groups: two examples of column density strengths possibly increasing or decreasing within 1 hr. 2012 March 27 group: represents an interesting pattern of column densities between orbital phases $135°$ and $145°$. This region appears to show the column density may be oscillating between two values, one around 3×10^{20} m^{-2} and the other being within 1σ of 0.

analysis could potentially provide constraints on the frequency and durations of these jet events. Now that JWST has demonstrated that it can detect Enceladus's vapor plume (Villanueva et al. 2023), future JWST observations could contribute a deeper understanding of the fluctuations of water-vapor content.

Appendix A
Mie Models

The first evidence of the water-vapor feature came from examining residuals of Enceladus plume spectra from Mie scattering models. Mie scattering models are used for various

applications including modeling coma particles from comets (Filacchione et al. 2020). In this study, the Mie models were utilized to model the crystalline water-ice 3.0 μm absorption feature in the particulate component of the Enceladus plume. We modeled a data set obtained from Hedman et al. (2009) containing spectra of effective altitudes above the surface of Enceladus processed from a subset of 14 spectral cubes observed in 2005.

In fitting these models, a slight peak appears in the 2.60–2.75 μm range in some of the spectra while usually showing up in spectra observed at lower altitudes. The upper panel in Figure 5 shows the best-fit Mie model for the plume spectra at an altitude of 35 km in the 2.50–3.70 μm range. The lower panel in Figure 5 shows the residual brightness produced by subtracting the Mie model from the plume spectra, which shows a clear peak. This finding prompted us to expand our analysis to a larger data set of VIMS spectral cubes and develop quadratic fitting models for isolating the water-vapor emission feature from the water-ice absorption spectra.
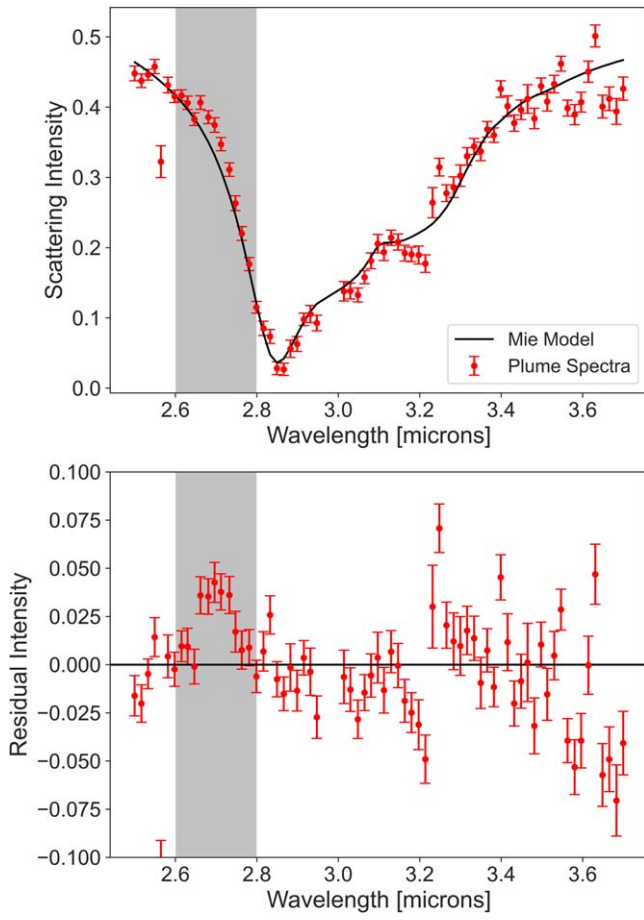
Figure 5. Modeling Enceladus plume spectra using Mie scattering theory. The processed plume spectra were obtained from Hedman et al. (2009). Upper panel shows the best-fit Mie model for plume spectra observed 35 km above the surface of Enceladus in the 2.5–3.7 μm wavelength range. Lower panel shows the resulting residual intensity after subtracting the Mie model from the spectra. The shaded regions on each plot highlight the wavelength band of interest, a near-infrared region that contains a water-vapor emission peak.

Appendix B
PSG

Table 2 shows the parameters used in this study to produce PSG models analyzed in Section 3.2. Due to the structure of Enceladus's plume and the composition of the plume material, we modeled the atmosphere of Enceladus as an expanding coma. Figure 6 shows the shift in spectral channels in Cassini-VIMS observations from 2005 to 2015. The shift is represented by ten PSG models of the water-vapor emission feature between 2.60 and 2.75 μm. This shift is documented in detail in Clark et al. (2018). The decrease in intensity over this time period is due to the increasing distance between the Sun and the Saturnian system as Saturn completes its 29 yr orbit.

Table 2
Planetary Spectrum Generator Parameters

Parameter	Value
Object	S-Enceladus
Viewing Geometry	Limb
Altitude	1000 km
Atmosphere	Expanding Coma
Activity[a]	3.63×10^{19} m^{-2}
Temperature[b]	70 K
Expansion Velocity[c]	780 m s^{-1}
Composition	GSFC[H2O]
Abundance	100%
Spectral Range	2.5–2.9 μm
Resolution (Resolving Power)[d]	300
Include Molecular Signatures	(Check)
Spectrum Intensity Unit	W sr^{-1} m^{-2} μm^{-1}

Notes.
[a] Column density estimate from Section 3.
[b] Estimated temperature of Enceladus's surface. This is different from the rotational temperature of water molecules as quoted in Villanueva et al. (2023).
[c] Expansion velocity value taken from Villanueva et al. (2023).
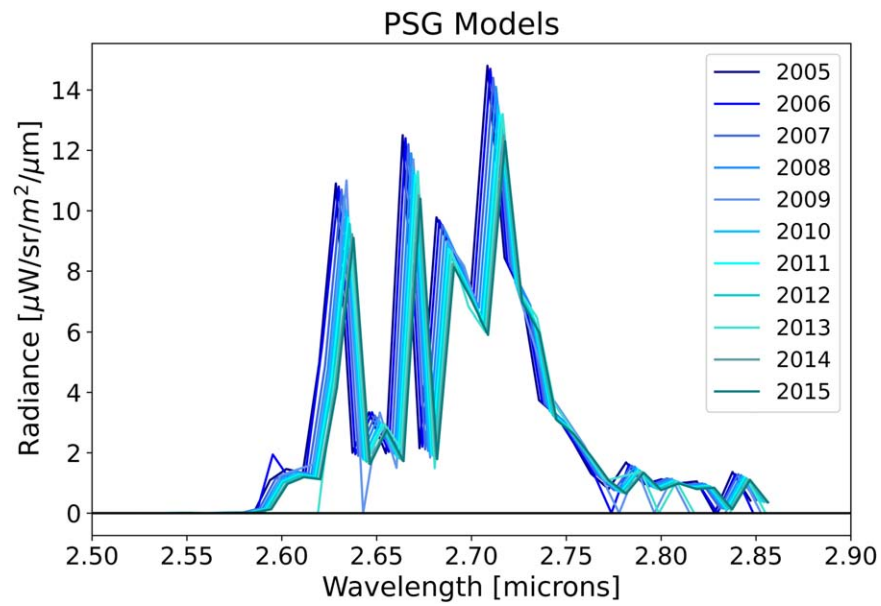[d] Resolving power value taken from Brown et al. (2004).

Figure 6. Theoretical spectral channel shift of the water-vapor emission feature in Cassini-VIMS observations from 2005 to 2015. Spectral shift values were taken from Clark et al. (2018), and the spectral models were produced using the PSG.

Appendix C
Column Density Plots

Similar to Figure 4, Figures 7 and 8 show the column density variations of the rest of the observation groups excluding the groups with only one spectral cube. Other details of these groups can be found in Table 1.
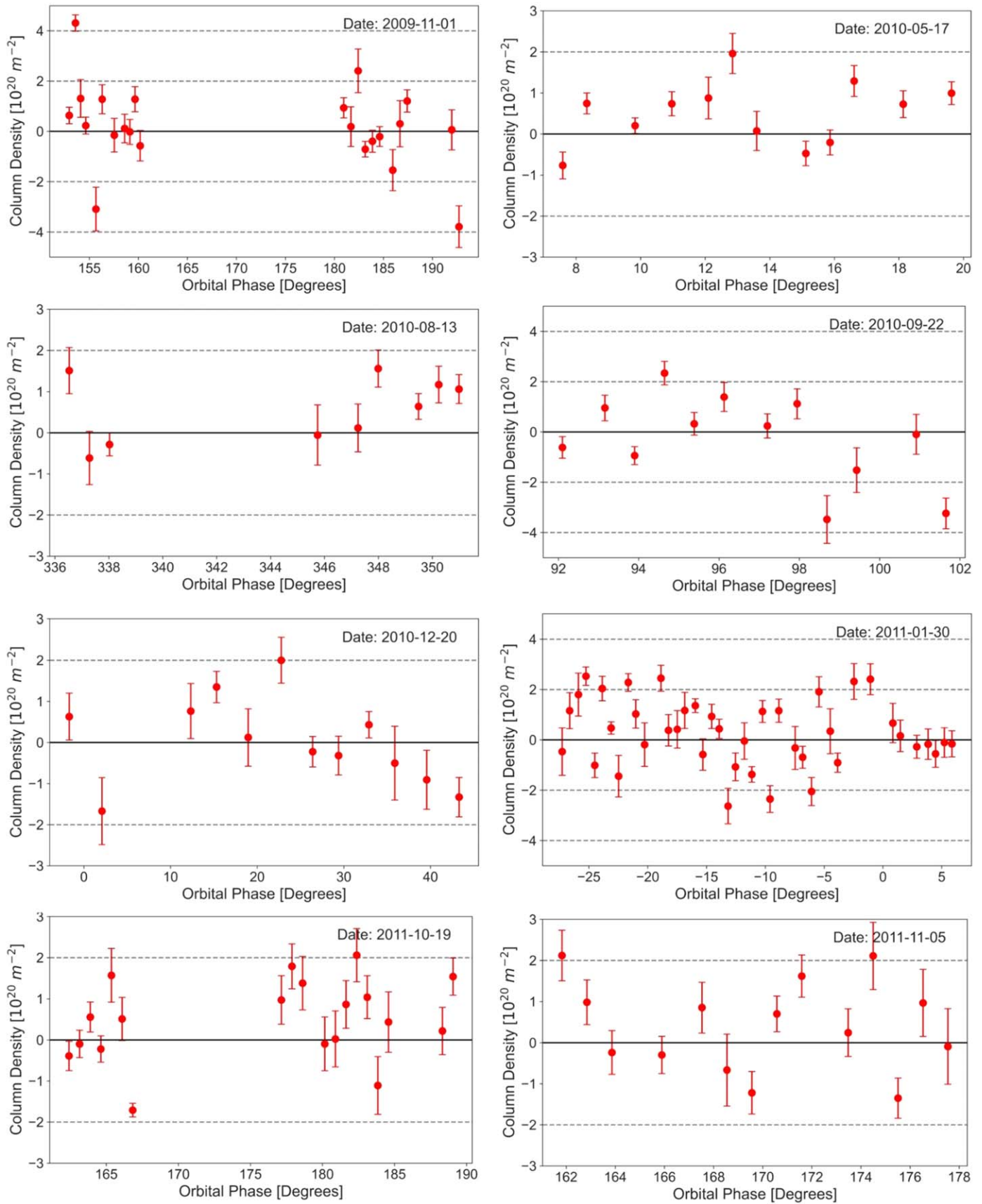
Figure 7. Column density variations for groups 2009 November 1 through 2011 November 5. Variations in groups 2005 November 27, 2007 September 30, and 2011 October 1 can be found in Figure 4.
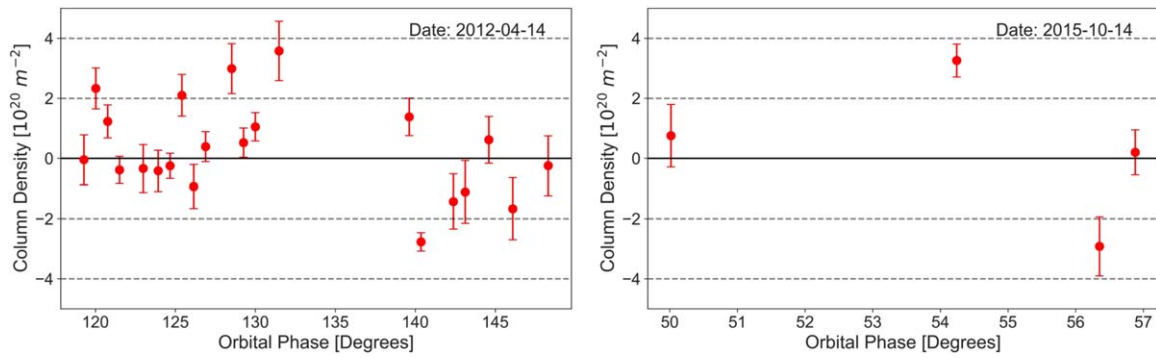
Figure 8. Column density variations for groups 2012 April 14 and 2015 October 14. Variations in group 2012 March 27 can be found in Figure 4.

Appendix D
Residuals

Figure 9 shows multiple residuals obtained from averaged spectra of spectral cubes with similar observation times (see Table 1). The spectral residuals shown are associated with column density uncertainties lower than 1.2×10^{19} m^{-2}. Figures 10 and 11 show individual spectral residuals for each observation group listed in Table 1.

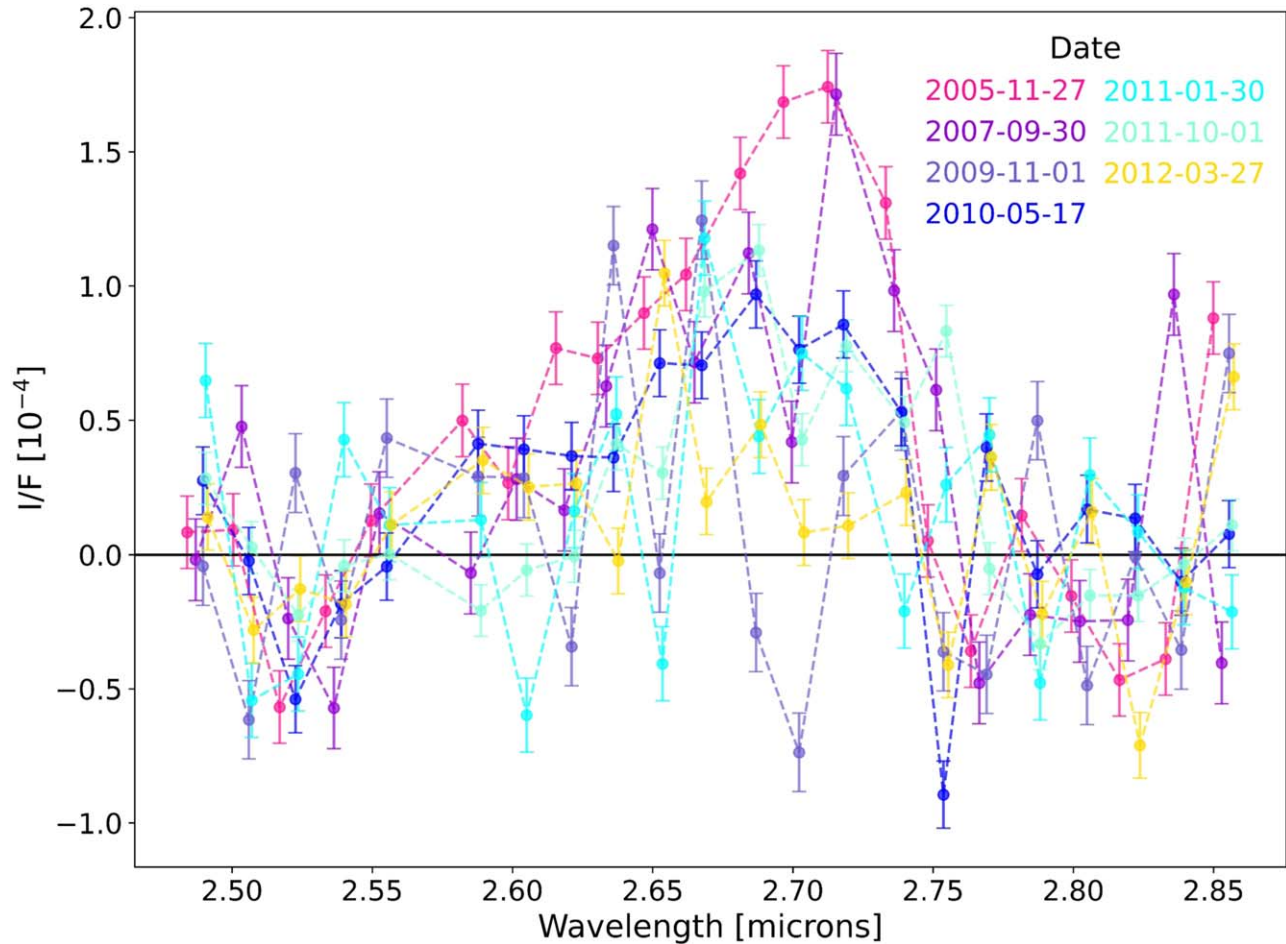**Figure 9.** The nonweighted average spectral residuals for observation groups with a column density error lower than 1.2×10^{19} m^{-2}. Each residual is colored by the date the observations were taken, corresponding to Figure 3.
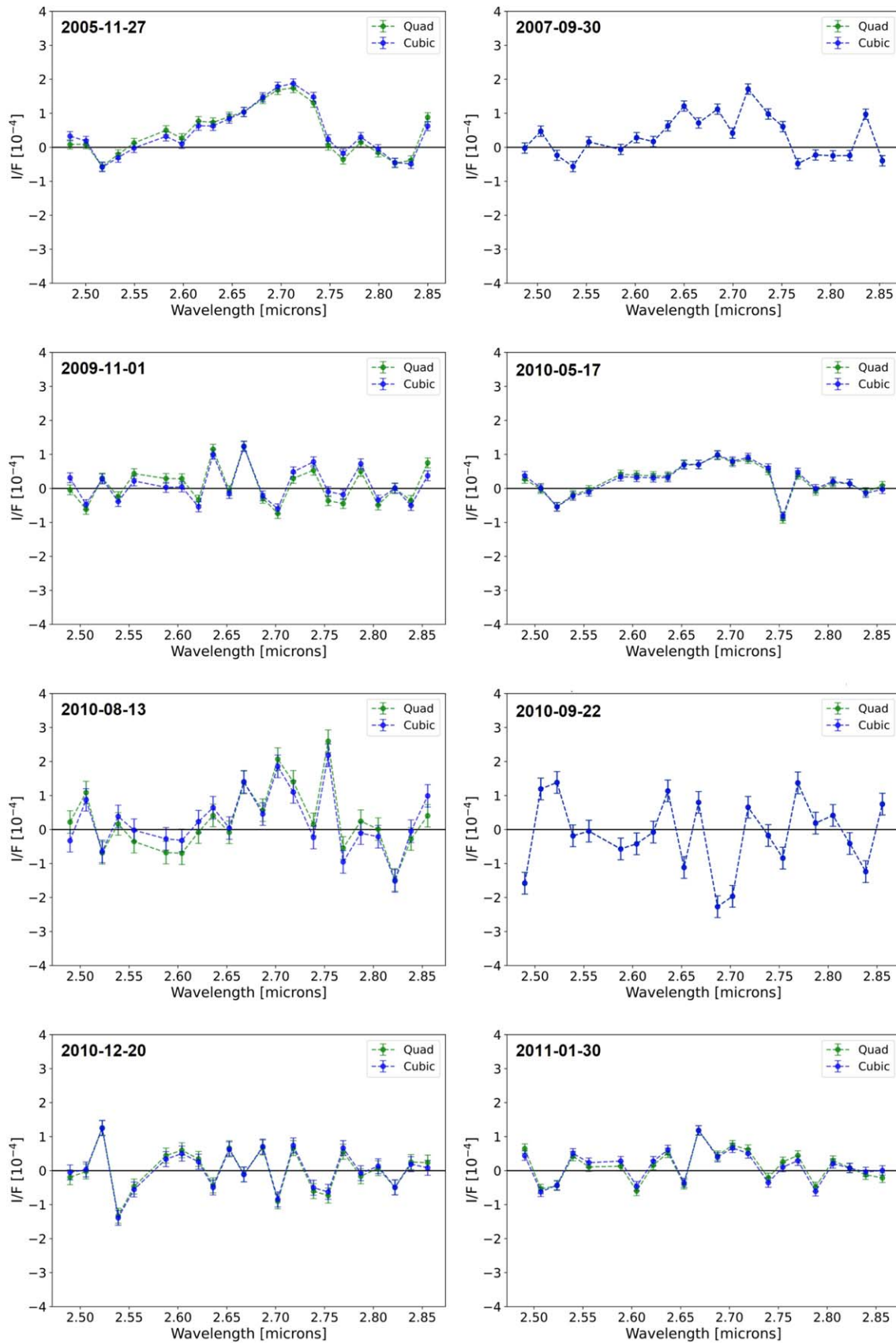
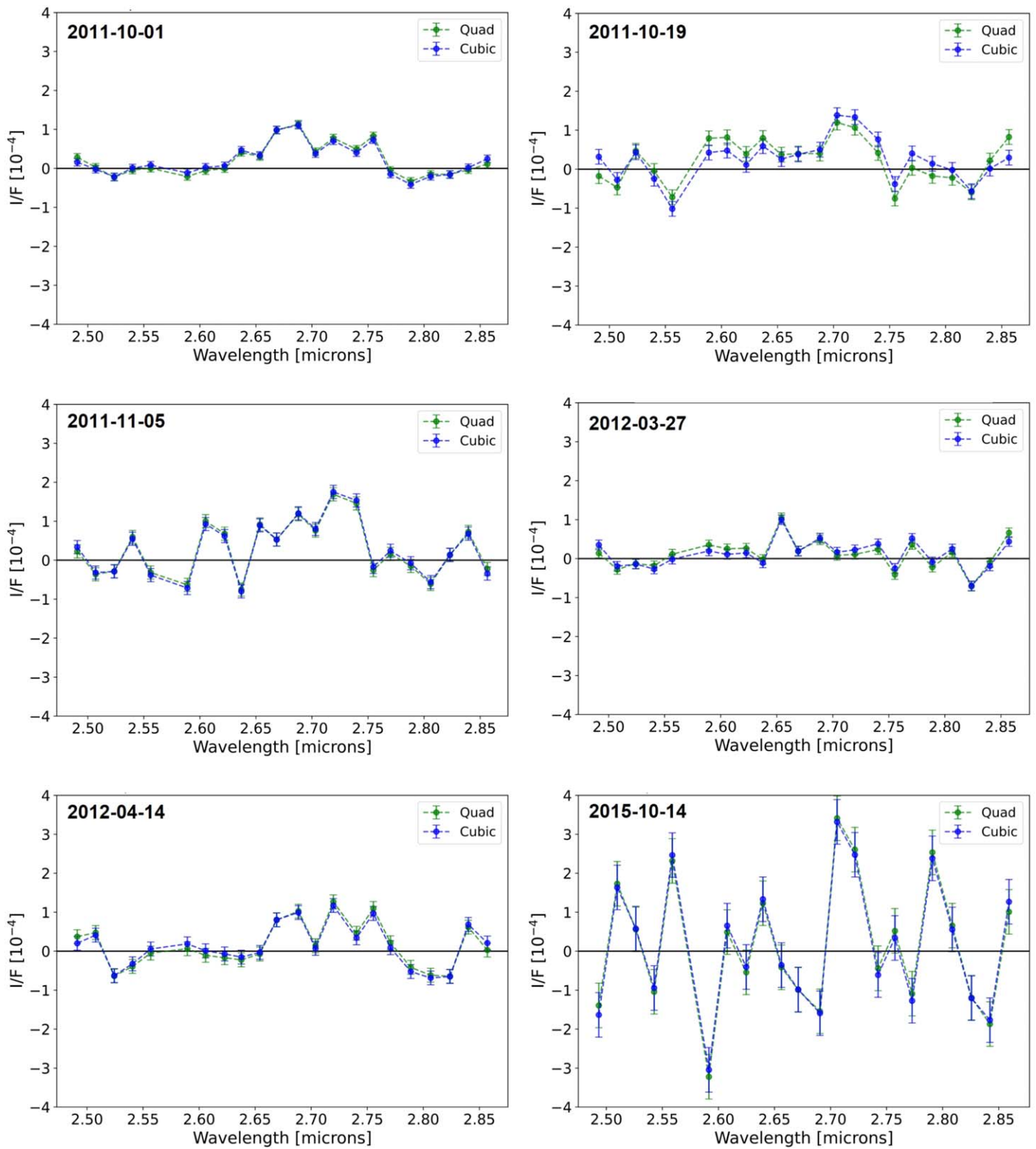**Figure 10.** Residual spectra for groups 2005 November 27 through 2011 January 30.

Figure 11. Residual Spectra for groups 2011 October 1 through 2015 October 14.

ORCID iDs

M. M. Hedman ⓘ https://orcid.org/0000-0002-8592-0812
G. Filacchione ⓘ https://orcid.org/0000-0001-9567-0055

References

Bockelée-Morvan, D., Debout, V., Erard, S., et al. 2015, A&A, 583, A6
Brown, R. H., Baines, K. H., Bellucci, G., et al. 2004, SSRv, 115, 111
Clark, R. N., Brown, R. H., Lytle, D. M., & Hedman, M. 2018, The VIMS Wavelength and Radiometric Calibration 19, Final Report, https://planetarydata.jpl.nasa.gov/img/data/cassini/cassini_orbiter/vims-calibration-files/clark-et-al_vims-radiometric-calibration-pds-2018-v2.0.pdf
Dhingra, D., Hedman, M. M., Clark, R. N., & Nicholson, P. D. 2017, Icar, 292, 1
Filacchione, G., Capaccioni, F., Ciarniello, M., et al. 2020, Natur, 578, 49
Goguen, J. D., Buratti, B. J., Brown, R. H., et al. 2013, Icar, 226, 1128
Hansen, C. J., Esposito, L. W., Colwell, J. E., et al. 2020, Icar, 344, 113461
Hedman, M. M., Gosmeyer, C. M., Nicholson, P. D., et al. 2013, Natur, 500, 182
Hedman, M. M., Nicholson, P. D., Showalter, M. R., et al. 2009, ApJ, 693, 1749
Hurford, T. A., Bills, B. G., Helfenstein, P., et al. 2009, Icar, 203, 541
Ingersoll, A. P., Ewald, S. P., & Trumbo, S. K. 2020, Icar, 344, 113345
Nimmo, F., Porco, C., & Mitchell, C. 2014, AJ, 148, 46
Portyankina, G., Esposito, L. W., Aye, K.-M., Hansen, C. J., & Ali, A. 2022, Icar, 383, 114918
Postberg, F., Clark, R. N., Hansen, C. J., et al. 2018, in Enceladus and the Icy Moons of Saturn, ed. P. M. Schenk et al. (Tucson, AZ: Univ. Arizona Press), 129
Saur, J., Schilling, N., Neubauer, F. M., et al. 2008, GeoRL, 35, L20105
Schenk, P., White, O. L., Byrne, P. K., & Moore, J. M. 2018, in Enceladus and the Icy Moons of Saturn, ed. P. M. Schenk et al. (Tucson, AZ: Univ. Arizona Press), 237
Sharma, H., Hedman, M. M., & Vahidinia, S. 2023, PSJ, 4, 108
Smith, H. T., Johnson, R. E., Perry, M. E., et al. 2010, JGRA, 115, A10252
Spencer, J. R., Nimmo, F., Ingersoll, A. P., et al. 2018, in Enceladus and the Icy Moons of Saturn, ed. P. M. Schenk et al. (Tucson, AZ: Univ. Arizona Press), 163
Teolis, B. D., Perry, M. E., Hansen, C. J., et al. 2017, AsBio, 17, 926
Thekaekara, M. 1973, in The Extraterrestrial Solar Spectrum, ed. A. Drummond & M. P. Thekaekara (Mount Prospect, IL: Inst. Environmental Sciences), 71
Villanueva, G. L., Hammel, H. B., Milam, S. N., et al. 2023, NatAs, 7, 1056
Villanueva, G. L., Smith, M. D., Protopapa, S., Faggi, S., & Mandell, A. M. 2018, JQSRT, 217, 86